

# Measuring the Electron Density Roughness of the D-Region Ionosphere

Cohen Morris B.<sup>1</sup> and Higginson-Rollins Marc Alexander<sup>1</sup>

<sup>1</sup>Georgia Institute of Technology

November 16, 2022

## Abstract

We present a method of characterizing the horizontal and vertical electron density roughness of the D-region ionosphere using Nationwide Differential GPS (NDGPS) transmitters as Low Frequency (LF; 30-300 kHz) and Medium Frequency (MF; 300-3000 kHz) signals of opportunity. The horizontal roughness is characterized using an amplitude cross-correlation method, which yields the correlation length scale metric. The vertical roughness is characterized using a differential phase height, which is needed to mitigate the effects of transmitter phase instability. The ranges and typical values of roughness metrics are investigated using data from several field campaign measurements. Finally, the roughness metrics for an NDGPS transmitter and VLF transmitter are compared. It is found that the roughness detected by the VLF transmitter is significantly smoother and demonstrates the utility of this method to complement traditional VLF measurements.

# Measuring the Electron Density Roughness of the D-Region Ionosphere

Marc A. Higginson-Rollins<sup>1</sup>, Morris B. Cohen<sup>1</sup>

<sup>1</sup>School of Electrical and Computer Engineering, Georgia Institute of Technology, 777 Atlantic Drive NW,  
Atlanta, GA 30332

## Key Points:

- A method for characterizing the horizontal and vertical electron density roughness of the D-region using LF/MF signals of opportunity is outlined.
- Field campaign data is used to investigate typical values of the horizontal and vertical roughness.
- The electron density roughness of the D-region is compared using a 25.2 kHz source and a 319 kHz source with similar paths.

---

Corresponding author: Marc Higginson-Rollins, [mahr3@gatech.edu](mailto:mahr3@gatech.edu)

## 13 Abstract

14 We present a method of characterizing the horizontal and vertical electron density  
 15 roughness of the D-region ionosphere using Nationwide Differential GPS (NDGPS) trans-  
 16 mitters as Low Frequency (LF; 30–300 kHz) and Medium Frequency (MF; 300–3000  
 17 kHz) signals of opportunity. The horizontal roughness is characterized using an ampli-  
 18 tude cross-correlation method, which yields the correlation length scale metric. The ver-  
 19 tical roughness is characterized using a differential phase height, which is needed to mit-  
 20 igate the effects of transmitter phase instability. The ranges and typical values of rough-  
 21 ness metrics are investigated using data from several field campaign measurements. Fi-  
 22 nally, the roughness metrics for an NDGPS transmitter and VLF transmitter are com-  
 23 pared. It is found that the roughness detected by the VLF transmitter is significantly  
 24 smoother and demonstrates the utility of this method to complement traditional VLF  
 25 measurements.

## 26 1 Introduction

27 The D-region of the ionosphere, which ranges from about 60-100 km, is too high  
 28 for continuous in-situ measurements, such as with high-altitude balloons, and too low  
 29 for satellite-based measurements. Molecular oxygen and nitrogen, nitric oxide, and other  
 30 atoms, such as sodium and calcium, constitute this layer of ionization (Nicolet & Aikin,  
 31 1960). The ionization in the D-region of the ionosphere is primarily due to Lyman- $\alpha$   
 32 radiation during the day and cosmic rays and Lyman- $\beta$  backscatter from the Earth’s hy-  
 33 drogen exosphere at night (Kotovsky & Moore, 2016). This ionization acts as a disper-  
 34 sive, anisotropic media that reflects lower frequency waves and attenuates higher frequen-  
 35 cies.

36 Since the D-region (and the ground) reflects lower frequency waves efficiently, the  
 37 region between the Earth and the D-region is often referred to as the “Earth-Ionosphere  
 38 Waveguide”. An effective and widespread method to study the D-region is through the  
 39 use of Very Low Frequency (VLF, 3–30 kHz) and Low Frequency (LF, 30–300 kHz) ra-  
 40 dio waves from man-made transmitters, (e.g. (Füllekrug et al., 2019)), or natural sources  
 41 (e.g. (McCormick et al., 2018)), due to the efficient reflection of waves that allow prop-  
 42 agation to global distances. As the frequency of the wave increase, the attenuation of  
 43 the reflected signal increases as well, (Bickel, 1957), as does the reflection height. Waves  
 44 between LF and Medium Frequencies (MF, 300–3000 kHz) reflect higher, with higher  
 45 attenuation, but still reflect within the D-region and can serve to complement VLF ob-  
 46 servations. Waves around 200–400 kHz have previously been used to monitor and study  
 47 the D-region, (Belrose et al., 1959; Bickel, 1957; Clarke, 1962; C. McKerrow, 1957; C. A. McK-  
 48 errow, 1960; Belrose & Thomas, 1968). (Higginson-Rollins & Cohen, 2017) found that  
 49 the United States Coast Guard’s (USCG) Nationwide Differential Global Position Sys-  
 50 tem (NDGPS) can be used as a signal of opportunity for studying the D-region and cap-  
 51 tures perturbations typically associated with the D-region. (Higginson-Rollins & Cohen,  
 52 2020) used NDGPS transmitters to study the effect of the August 2017 “Great Amer-  
 53 ican” solar eclipse on D-region electron density.

54 The “small-scale roughness” of the electron density of the D-region is not well un-  
 55 derstood. The bulk of VLF research studying the D-region has been focused on global  
 56 or regional studies, and typically all assume a stratified ionosphere. Some previous work  
 57 done at VLF, e.g. (Lay & Shao, 2011b, 2011a; Füllekrug et al., 2015), examined more  
 58 localized variation, but these studies are by no means exhaustive and fail to truly char-  
 59 acterize roughness on a scale less than 10-100 km, particularly under ambient conditions.  
 60 Early work done using the partial reflection technique touches on the idea of small-scale  
 61 roughness, but the work was limited in scope and focused on understanding the mech-  
 62 anism of weak partial reflections rather than characterizing the roughness, e.g. (Shapiro,  
 63 1973), (Mathews et al., 1973), and (W. K. Hocking, 1979). This paper will outline a tech-

64 nique for studying the small-scale electron density roughness of the D-region using NDGPS  
 65 transmitters. Metrics for determining the horizontal and vertical roughness will be de-  
 66 scribed and applied to field campaign data.

## 67 2 Data Collection and Interpretation

### 68 2.1 LF AWESOME Receivers

69 The data in this paper was collected using the LF AWESOME Receiver (Cohen  
 70 et al., 2018). This instrument consists of two orthogonal air-core loop antennas and has  
 71 a sampling rate of 1 MHz, giving a band-pass of approximately 0.5–470 kHz, sensitiv-  
 72 ity up to  $0.03 \text{ fT}/\sqrt{\text{Hz}}$  at 30 kHz and  $0.1 \text{ fT}/\sqrt{\text{Hz}}$  at 300 kHz, and RMS timing ac-  
 73 curacy of 15–20 ns for the RMS accuracy of all the timing pulses that make up the 1  
 74 MHz clock (implying precise phase estimation of  $<1.5$  degrees at 300 kHz), there is no  
 75 frequency drift/offset in the clock detectable with 0.5 part-per-billion resolution. The  
 76 Georgia Tech Low Frequency Lab currently operates a network of 11 receivers through-  
 77 out the United States and Japan. The two receivers used for this paper are located at:  
 78 1) Baxley, Georgia, [31.8767° N, 82.3621° W], 2) Pisgah Astronomical Research Insti-  
 79 tute (PARI), North Carolina, [35.1996° N, 82.8719° W].

### 80 2.2 NDGPS Transmitters

81 The NDGPS network consists of 33 sites which broadcast, between 285–325 kHz,  
 82 the difference between a known, fixed location and the received GPS coordinates to im-  
 83 prove the accuracy of commercial GPS to centimeter accuracy (D. Last & Poppe, 1996;  
 84 J. Last & Poppe, 1997; Wolfe et al., 2000). From extensive measurements using multi-  
 85 ple transmitters and receivers, it has been found that the transmitter clocks drift, which  
 86 causes phase instability, limiting the usefulness of the phase data. Thus, in this paper,  
 87 only amplitude metrics are considered. Three transmitters will be used for this paper:  
 88 1) New Bern, North Carolina, [35.1750° N, 77.0485° W], 2) Tampa, Florida, [27.8502°  
 89 N, 82.5324° W], and 3) Bobo, Mississippi, [34.1152° N, 90.6912° W]. Respectively, the  
 90 transmitters have a baud rate of 100 bits-per-second (BPS), 200 BPS, and 200 BPS, and  
 91 a center frequency of 294 kHz, 312 kHz, and 297 kHz.

### 92 2.3 Data Interpretation

93 The receiver collects broadband data for both the North/South (N/S) and the East/West  
 94 (E/W) channel. A synchronized minimum-shift keyed (MSK) demodulation is then ap-  
 95 plied to the broadband data, which converts the MSK modulated transmitter signal into  
 96 a quasi-CW (continuous wave) signal. The result is that the horizontal magnetic flux den-  
 97 sity of a narrowband transmitter can be represented by the amplitude and (carrier) phase  
 98 of the N/S and E/W channel. These four values can be written as two separate com-  
 99 plex phasors that defines an ellipse centered at the origin. Measures can be derived from  
 100 the resulting ellipse and include major axis length, minor axis length, right-hand circular  
 101 polarization (RHCP), left-hand circular polarization (LHCP), ellipticity, tilt angle,  
 102 and start phase. Synchronized MSK demodulation and the polarization ellipse method  
 103 are both covered in great detail by (Gross et al., 2018). The work in this paper will pri-  
 104 marily focus on the major axis length and the minor axis length. These parameters cor-  
 105 respond to the transverse magnetic (TM) and transverse electric (TE) modes of the mag-  
 106 netic field respectively.

## 107 3 Characterizing Roughness

108 To determine the location and size of an active scattering region contributing to  
 109 the total field at a receiving point from a surface illuminated by a source the commonly

110 accepted answer is the *Fresnel zones*, specifically the first Fresnel zone. At oblique in-  
 111 cidence angles, such as in the case of a radio wave reflection from the lower ionosphere,  
 112 this answer becomes less rigorous, but has been used in other works in this context, such  
 113 as in (Lay & Shao, 2011b) and (Lay & Shao, 2011a).

114 The basic idea of the first Fresnel zone is as follows. Imagine a surface, such as the  
 115 D-region, illuminated by a transmitter that in turn reflects radio waves, which are de-  
 116 tected by a receiver at some distance. The locus of all points on the reflecting surface  
 117 that generate a reflection that arrives at the receiver with a constant phase difference,  
 118  $\delta$ , with respect to the direct radiation along  $d$  is given by Equation 1. In Equation 1,  $R_1$   
 119 and  $R_2$  are the distances of the up going and down going rays and  $\delta$  is the constant phase  
 120 difference. If  $\delta$  is incremented in steps of  $\frac{\lambda}{2}$ , concentric ellipses with phase differences of  
 121  $\pi$  will arise. This effectively creates rings of alternating constructive and destructive phase  
 122 interference, which form ellipses on the D-region, where the first Fresnel zone will be de-  
 123 fined as the area inside the first ellipse where the locus of all points will constructively  
 124 interfere with a phase of  $\pi$ . In general, the first Fresnel zone, or the first ellipse on the  
 125 surface, has the greatest contribution to the received signal because of the following rea-  
 126 sons: 1) the concentric ellipses, after the first Fresnel zone, have a decreasing area and  
 127 thus decreasing contribution to the received signal, 2) the alternating concentric ellipses  
 128 of constructive and destructive interference, though not identical in size, approximately  
 129 cancel out. For a thorough reference text on Fresnel zones and related topics refer to (P.  
 130 Beckmann & A. Spizzichino, 1963).

$$R_1 + R_2 - d = \delta \quad (1)$$

131 In the case of a receiver detecting the signal from an LF/MF transmitter, such as  
 132 an NDGPS transmitter, at oblique incidences, the first Fresnel ellipse will appear as an  
 133 ellipse that becomes more elongated as the distance between the transmitter and receiver  
 134 increases. The direction along the path of propagation, or rather the direction towards  
 135 the receiver from the transmitter, is called the *radial* direction. The direction perpen-  
 136 dicular to the direction of propagation is called the *transverse* direction. The radial and  
 137 transverse first Fresnel radii can be calculated for varying propagation distances. For ex-  
 138 ample, assume a propagating wave has a frequency of 300 kHz, a reflection height of 90  
 139 km, and a propagation distance of 600 km. The radial radius would be about 43.2 km  
 140 and the transverse radius would be 12.5 km. If the propagation distance is increased to  
 141 1200 km, the radial radius would increase to about 115.3 km and the transverse radius  
 142 would increase to 17.4 km. Thus, the active scattering region, i.e. the first Fresnel zone,  
 143 grows with distance and can become quite large at longer distances. It should also be  
 144 noted that, at distances of about 700–1200 km, the first skywave is the dominant mode.  
 145 This means that, at these distances, the first Fresnel zone is effectively a “patch” of the  
 146 D-region that is being probed by the LF/MF waves with minimal contributions from higher  
 147 order modes. The metrics discussed in the next sections will focus on describing the “ver-  
 148 tical” and “horizontal” roughness of the D-region by exploiting this concept, specifically  
 149 that the patch of the D-region being probed is more or less equivalent to the Fresnel zone  
 150 at the center of the propagation path between the transmitter and receiver.

151 The remainder of this section outlines the two key metrics that will be used to mea-  
 152 sure the roughness of the D-region electron density in terms of the vertical, differential  
 153 phase height, and horizontal roughness, correlation length scale. Both these metrics ex-  
 154 ploit the concept of the first Fresnel zone, which is the patch that is being probed by the  
 155 transmitter.

156

### 3.1 Vertical Roughness

157

158

159

160

161

162

163

164

165

A group of methods used to estimate the reflection height of a low frequency wave from the D-region using phase data are called *virtual reflection height* methods. A summary of these methods can be found in (Piggott et al., 1965). This section will focus on one method in particular called the *phase height* method and is described by  $h_1$  in Equation 2, where  $\lambda$  is the wavelength,  $I$  is the angle of incidence from the vertical plane pointed from the ground to the ionosphere,  $\theta_g$  is the phase difference between the up-going and down-coming waves observed at the ground, and  $M$  is simply an arbitrary integer. It is important to note, that the solution of Equation 2 is not unique and is dependent on the choice of  $M$ .

$$\frac{-4\pi h_1}{\lambda} \cos I = (2M + 1)\pi + \theta_g \quad (2)$$

166

167

168

169

170

171

172

173

174

175

176

177

However, the NDGPS transmitters being used as a signal of opportunity suffer from clock instabilities that cause ramping in the phase data. This is problematic since the possible equivalent reflection height techniques from (Piggott et al., 1965) are all reliant on phase data. To cope with this problem, a modification has been made to the *phase height* technique described in Equation 2. First, envision a propagation scheme, like the one depicted in Figure 1, where a transmitter, left, is detected by two receivers, right, at some distance  $d_1$  and  $d_2$  away. Each wave, depicted in the figure as a ray, propagates in a similar path and reflects off the D-region, seen as the blue region above, at some height,  $h_1$  and  $h_2$  respectively, with some angle of incidence,  $\theta_1$  and  $\theta_2$ . An important assumption made here is that the receivers are placed sufficiently far from the transmitter, e.g. approximately 700 km to 1200 km, in order to ensure that only one skywave is propagating.

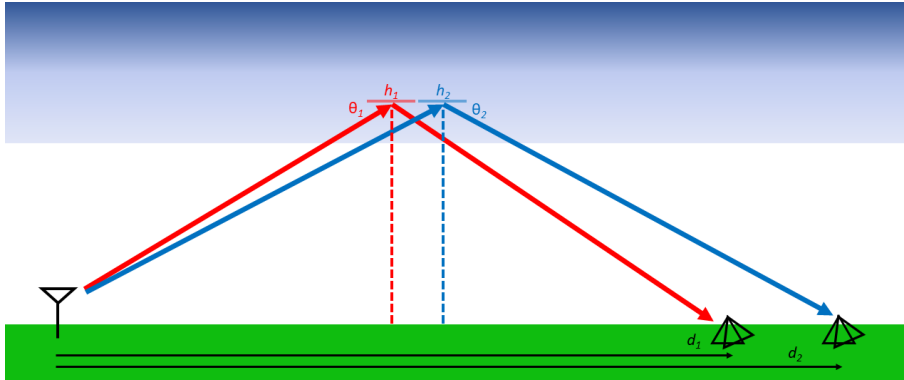


**Figure 1.** Example propagation scheme of a transmitter (left) and two closely spaced receivers (right) with the waves reflecting off of the D-region.

178

179

180

181

182

183

184

185

186

187

With two receivers, there are now phase measurements at two different locations. This will be the key difference between the *phase height* method described in Equation 2 and what will now be called the *differential phase height*. Equation 3 describes what happens when the two phase values at each receiver,  $\phi_1$  and  $\phi_2$ , are subtracted from each other. Each phase value can be broken into three parts: 1) the contribution of the transmitter source ( $\phi_{n,source}$ ), 2) the ionospheric and path contribution ( $\phi_{n,ionosphere}$ ), and 3) the contribution from nearby scattering ( $\phi_{n,site}$ ). Between the two receivers, the contribution from the transmitter source should be identical and thus, when subtracted, should cancel completely, which effectively eliminates the “phase ramping” described above. The remaining phase elements are described in Equation 4, where  $\phi_{\Delta,ionosphere}$  is the differ-

188 ence in the ionospheric, and path, contribution,  $\phi_{noise}$  is the contribution of any time  
 189 varying noise (e.g. receiver noise), and  $\phi_{bias}$  is the contribution of any “constant bias”,  
 190 such as nearby scattering from geographical features or buildings.

$$\phi_{\Delta} = \phi_1 - \phi_2 = \phi_{1,source} + \phi_{1,ionosphere} + \phi_{1,site} - \phi_{2,source} + \phi_{2,ionosphere} + \phi_{2,site} \quad (3)$$

$$\phi_{\Delta} = \phi_{\Delta,ionosphere} + \phi_{noise} + \phi_{bias} \quad (4)$$

191 In Equation 2, the right-hand side can be enclosed into a variable, such as Equa-  
 192 tion 5. Given the right selection of  $M$ , the phase values from Equation 4 and Equation  
 193 5 will be equal,  $\phi_{\Delta} = \phi'_{\Delta}$ .

$$\phi'_{\Delta} = (2M + 1)\pi + \theta_g \quad (5)$$

194 Thus, we can then substitute Equation 4 into Equation 2 and solve for the equiv-  
 195 alent reflection height, yielding Equation 6. Where  $\lambda$  is the wavelength,  $\theta_i$  is the angle  
 196 of incidence (in radians), and  $\phi_{\Delta}$  is the phase from Equation 4.

$$H = -\frac{\phi_{\Delta}\lambda}{4\pi \cos \theta_i} \quad (6)$$

197 Next, the metric we are interested in is a *relative change* in phase height, rather  
 198 than an absolute metric. Thus, the mean phase height,  $\bar{H}$ , is subtracted, which yields  
 199 a normalized relative phase height,  $\Delta h$ , as in Equation 7. It should be noted that be-  
 200 cause of this normalization, the integer choice,  $M$ , from Equation 5 becomes irrelevant.  
 201 This normalized, differential phase height is the final metric of interest. However, to mea-  
 202 sure its variation, the *root-mean-squared* of a subset time series of normalized differen-  
 203 tial phase height values is calculated, using Equation 8, to measure the vertical varia-  
 204 tion in the D-region.

$$\Delta h = H - \bar{H} \quad (7)$$

$$\sigma_{RMS} = \sqrt{\frac{1}{N} \sum_{n=1}^N |\Delta h|^2} \quad (8)$$

205 The values for the wavelength,  $\lambda$ , and phase,  $\phi_{\Delta}$ , are known, however, the angle  
 206 of incidence,  $\theta_i$ , is still an unknown. Assuming a spherical Earth, a formula for the an-  
 207 gle of incidence based on the geometry of the problem can easily be solved using Equa-  
 208 tion 9, where  $R_e$  is the radius of the earth in meters,  $h_n$  is the reflection height in met-  
 209 ers, and  $d_n$  is the distance from the transmitter to the receiver in meters. The subscript  
 210  $n$  indicates the receiver number. The resulting angle of incidence,  $\theta_{i,n}$ , is in radians. The  
 211 formula on the right hand side is the angle from the vertical axis, the complementary  
 212 angle of the angle of interest. Thus, the angle is subtracted from  $\frac{\pi}{2}$ , which yields an an-  
 213 gle of incidence that can be used in Equation 6.

$$\theta_{i,n} = \frac{\pi}{2} - \arctan \frac{R_e \sin \frac{d_n}{2R_e}}{h_n + R_e(1 - \cos \frac{d_n}{2R_e})} \quad (9)$$

214 In Equation 9, there is still one unknown: the reflection height,  $h_n$ . However, only  
 215 the *relative change* in this variable is of interest. Thus, a best guess value for  $h_n$  is used  
 216 and left constant. This approximation results in a small error that decreases as prop-  
 217 agation distance increases. For example, if the reflection height is assumed to be 90 km  
 218 with a nighttime range of reflection heights of 85 – 95 km for a wave at 300 kHz. For  
 219 a propagation range of 900 km the error, that is the difference between the chosen value  
 220 and the bounds, is  $\theta_{error,i} \approx \pm 0.6^\circ$ .

221 An additional consideration for the use of Equation 6 is that, although there is only  
 222 one angle of incidence in the formula, there are actually two angles of incidence for the  
 223 two receivers being used. Two possible solutions to this problem are: 1) to take the mean  
 224 value of the two angles of incidence, 2) to pick one angle of incidence and use it. In the  
 225 context of this problem, the receiver spacing is often quite small,  $< 10\lambda$ , and if it's cho-  
 226 sen to be closer to  $\approx \lambda$ , then the error in the angle of incidence, if only a fixed value is  
 227 used, drops drastically. At a propagation distance of 900 km, the difference between two  
 228 receivers spaced one wavelength apart, with identical reflection heights, is only  $\theta_{error,i} \approx$   
 229  $0.01^\circ$ . Thus, this error becomes negligible under the right circumstances.

230 In conclusion, to measure the vertical roughness, or variability, of the D-region the  
 231 *differential phase height* method described above will be used to track the relative change  
 232 in phase height. Equation 6 is used to calculate the differential phase height using a fixed  
 233 value of angle of incidence, calculated using Equation 9, where an initial reflection height  
 234 of 90 km is used and kept constant. The resulting value is normalized using Equation  
 235 7 and then the root-mean-squared value is calculated from a subset of the time series  
 236 using Equation 8. The final metric describes the variability in the vertical phase height  
 237 between two “patches”, Fresnel zones, reflecting off the D-region.

### 238 3.2 Horizontal Roughness

239 The second component of characterizing the electromagnetic roughness of a sur-  
 240 face is determining the “horizontal roughness”. A common technique for characterizing  
 241 spatial variability, which can be applied to this problem, is called *cross-correlation anal-*  
 242 *ysis*. Variants of this method are widely used to solve problems in different remote sens-  
 243 ing fields. The work by (J. Doviak et al., 1994), and citations within, used spaced receiver  
 244 models and cross-correlation analysis to study atmospheric turbulence and wind param-  
 245 eters. A paper by E. N. Bramley, (Bramley, 1951), similar to the paper by (Briggs et  
 246 al., 1950), summarizes the use of a cross-correlation analysis technique on the reception  
 247 of radio waves from the ionosphere for two closely spaced aerial antennas, such as two  
 248 antennas on an airplane, for various conditions, such as whether there is a steady sig-  
 249 nal present or not. This work was expanded on by (Lindner, 1975b) and (Lindner, 1975a)  
 250 to, using the partial reflection technique, understand the angular spread of down com-  
 251 ing reflected waves, the coherence ratio, and the scale/size of reflecting ionospheric ir-  
 252 regularities. The work by (Wernik et al., 1983) used spaced receivers to study turbulent  
 253 ionospheric irregularities, specifically the mean drift velocity and direction, the charac-  
 254 teristic random velocity, the spatial scales of the irregularities, and the orientation of the  
 255 irregularities. Cross-correlation analysis has been successfully used in similar remote sens-  
 256 ing fields and can be applied to measure the spatial roughness of the D-region electron  
 257 density.

258 The primary metric derived from cross-correlation analysis is the *correlation length*  
 259 *scale*. The correlation length scale is a statistical measure that describes the spatial vari-  
 260 ance of a surface. In the context of this work, the correlation length scale will be used  
 261 to measure the spatial variance in the amplitude of a wave reflecting from the ionosphere.

262 It is well established in literature that the correlation length scale measured on the  
 263 ground can be used as a proxy for the scale of a perturbation or to estimate the angu-  
 264 lar spread of the scattering from a surface, (Ratcliffe, 1956). When the ionosphere is smooth,

265 the reflection will be *specular* and remain a narrow beam. As the roughness increases,  
 266 the down coming ray becomes more diffuse and becomes a wider “cone” instead of a nar-  
 267 row beam. Thus, as the roughness of the surface increases in relation to the wavelength  
 268 being used, the measured correlation length scale of should increase as well.

269 The correlation length scale is calculated as follows. First, the simultaneous am-  
 270 plitude data being analyzed (e.g. N/S amplitude, E/W amplitude, major axis length,  
 271 or minor axis length) from multiple receivers is aggregated, such as in Equation 10, where  
 272 each variable represents the time series of the metric being analyzed. In this case, the  
 273 time series may be the complete time series of the data collected during the campaign  
 274 or a windowed subset of it.

$$\vec{x} = [x_1(t), x_2(t), \dots, x_d(t)] \quad (10)$$

275 Once the data has been aggregated, the data from each receiver is normalized in-  
 276 dividually by calculating the *Z-score*, Equation 11, where  $\mu_x$  is the mean and  $\sigma_x$  is the  
 277 standard deviation.

$$\bar{x} = \frac{x - \mu_x}{\sigma_x} \quad (11)$$

278 Using the normalized values, the cross-correlation is calculated between each pair  
 279 of receiver metrics using Equation 12. Where  $x_{n+m}$  is one receiver site metric at time  
 280  $t = n + m$  and  $y_m^*$  is the complex conjugate of the other receiver site metric at time  
 281  $t = m$ . The result from Equation 12 is then normalized using Equation 13.

$$\hat{R}_{xy}(m) = \begin{cases} \sum_{n=0}^{N-m-1} x_{n+m} y_n^*, & m \geq 0, \\ \hat{R}_{yx}^*(-m), & m < 0. \end{cases} \quad (12)$$

$$\hat{R}_{xy,coef}(m) = \frac{1}{\sqrt{\hat{R}_{xx}(0)\hat{R}_{yy}(0)}} \hat{R}_{xy}(m) \quad (13)$$

282 The result of this calculation is used to find the *maximum* value of the *absolute* value  
 283 of each receiver pair combination. This results in a diagonal matrix of size  $D \times D$  where  
 284 the diagonal values are equal to approximately 1. Each point in this matrix corresponds  
 285 to a specific receiver spacing. Figure 2 illustrates the receiver spacing configuration for  
 286 a radial propagation scheme. A transmitter, on the left, is transmitting a wave that re-  
 287 flects off the ionosphere, middle of figure, and is detected by some number of receivers,  
 288 on the right. The receivers are located at a distance,  $d_{1,2,\dots}$ , from the transmitter. The  
 289 spacing between the receivers can be calculated in two ways: 1) the spacing between the  
 290 midpoints of the propagation paths,  $L'$ , or 2) the ground spacing,  $L$ . Each element of  
 291 the calculated diagonal matrix above has an equivalent diagonal matrix with elements  
 292 corresponding to the spacing using either  $L'$  or  $L$ . For this work, the ground spacing of  
 293 the receivers,  $L$ , is exclusively used in order to match the simulated results in the next  
 294 section.

295 In general, the exact cross-correlation point is not captured, so an exponential fit,  
 296 like the one in Equation 14, is used to approximate it. In Equation 14, “A” and “B” are  
 297 coefficients and generally  $A \approx 1$ . Figure 3 shows an example of this process. The left  
 298 panel shows the major axis, or  $H_\phi$ , correlation length scale. The blue square points are  
 299 cross-correlation values for each pair of receivers. The black line is the exponential fit  
 300 for the blue squares and the red horizontal line is the  $e^{-1}$  point. The point at which these  
 301 two lines intersect is the correlation length scale. The same plot is shown in the right  
 302 panel for the minor axis,  $H_\theta$ .

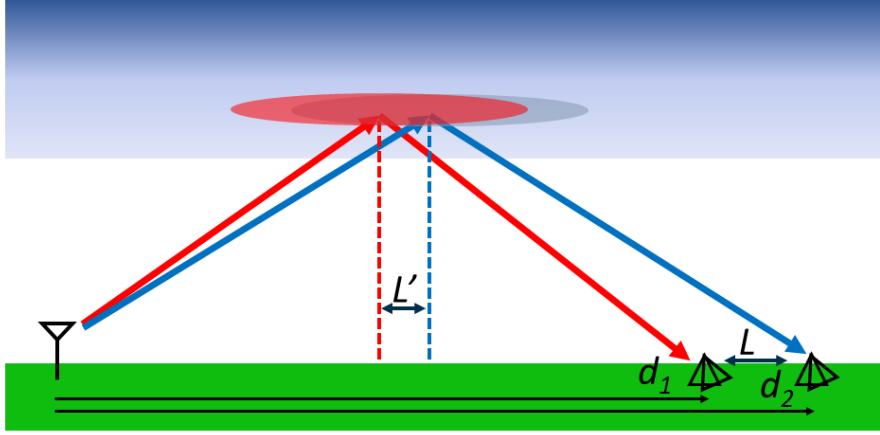


**Figure 2.** Example propagation scheme of a transmitter (left) and two closely spaced receivers (right) with the waves reflecting off of the D-region.

$$\hat{R}'(x) = A \exp^{Bx} \tag{14}$$

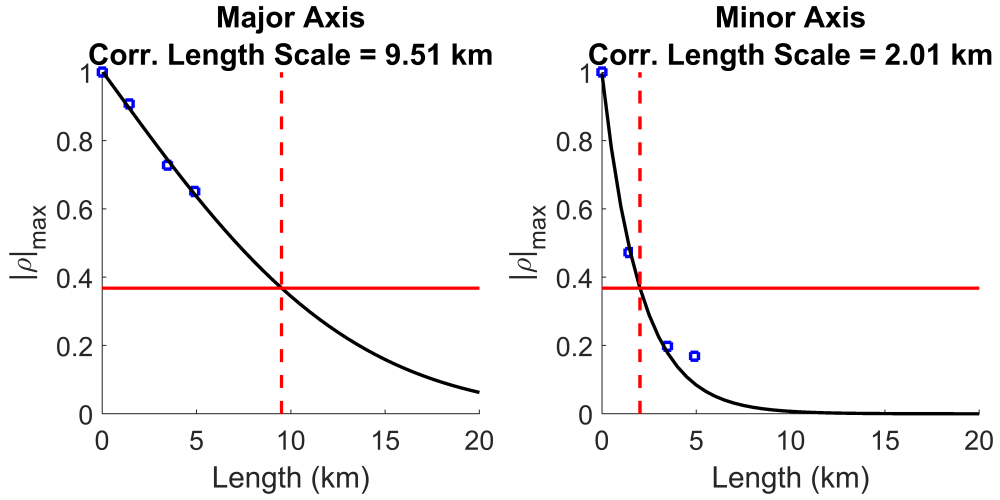


**Figure 3.** Example of estimating the correlation length scale using an exponential fit. The left panel shows the major axis cross-correlation values and the minor axis shows the minor axis values.

#### 4 Field Campaign Data Analysis

With the two roughness metrics identified, the correlation length scale and the RMS height variation, field campaign data was collected. The collected field campaign data will be presented below. The roughness metrics will be applied to the data and discussed. Finally, comparisons will be made to VLF transmitters.

303  
304  
305  
306  
307

308

#### 4.1 Field Campaigns

309

310

311

312

313

314

315

316

317

The D-region is non-stationary and fluctuates on a very quick timescale at night-time, e.g. 5–25 minutes. Early partial reflection measurements had difficulty dealing with this issue when using amplitude statistics to study D-region scattering, (W. Hocking, 1987). Thus, receiver spacing and geometry, i.e. simultaneous spatial sampling of the ionosphere, will be critical in accurately measuring the roughness of the D-region. Two primary considerations will have to be taken into account: 1) measurements should be oriented transverse or radial to the propagation path with little deviation, 2) the transmitter-receiver propagation distances should be limited to approximately 600–1200 km to fall in the propagation region dominated by the first skywave.

318

319

320

321

322

323

324

325

326

327

328

329

330

331

332

333

Several field measurements were made over the course of 2019. In each field campaign, some number of mobile receivers were deployed sequentially in a predetermined location, with permission from the property owner, such as a farm, and data was collected for some period. The data collected at each site is truncated to maximize the simultaneous data. Table 2 summarizes the completed field campaigns, where spacing from reference indicates the distance from a chosen reference site. All the field campaigns were conducted near the permanent receiver site located at Baxley, Georgia, [31.8767° N, 82.3620° W] indicated by the blue dot in Figure 4. This site is located at the “bottom” of what is called the *Southeast Array*, indicated by the black dots in the figure. The red dots in Figure 4 indicate the location of each transmitter used for this work. The red lines show the great circle paths (GCP) from the transmitter to the permanent receiver site in Baxley (GA). Table 1 summarizes the red transmitter-receiver paths shown in the figure, where the distances listed are from the transmitter to the permanent Baxley (GA) receiver. The receivers were arranged in a predominantly North-South orientation to capture data from several transmitters in a combination of “radial” and “transverse” paths, as depicted in Figure 5 where the arrow indicates the direction towards the transmitter being detected.

**Table 1.** Summary of the transmitters and transmitter-receiver path geometries from the completed field campaigns.

Transmitter	Coordinates	Frequency (kHz)	Distance (km)	Orientation
Detroit (MI)	42.2972°N, 83.0952° W	319	1158.3	Radial
English Turn (LA)	29.8783°N, 89.9417° W	293	757.7	Transverse
Tampa (FL)	27.8502°N, 82.5325° W	312	446.6	Radial
Card Sound (FL)	25.4317°N, 80.4663° W	314	737.9	Radial

**Table 2.** Summary of the field campaigns conducted in 2019 where the spacing from reference is the distance between each receiver site from a fixed reference and the total time refers to the total time of simultaneous data collection.

Date	Number of Receivers	Spacing from Reference (km)	Total Time (Hours)
01/14/19	3	2.5, 5	0.777
01/14/19	3	5, 10	0.540
06/13/19	3	2.5, 5	0.432
06/13/19	3	2.5, 1.4	0.684
08/22/19	4	7.2, 1.4, 4.9	1.504
09/06/19	3	1.4, 4.9	3.983
09/07/19	5	7.3, 8.3, 8.6, 12	5.893

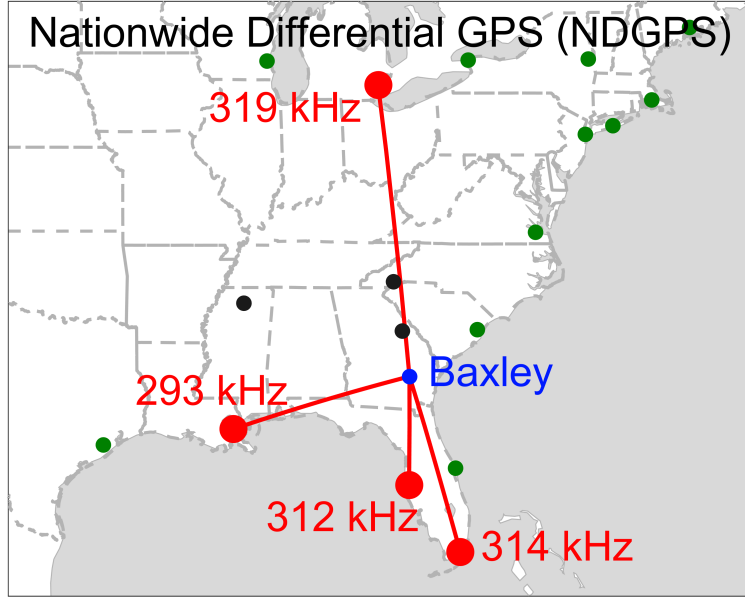


**Figure 4.** Map showing the transmitter-receiver paths for the completed campaigns. The receiver site is indicated by the blue dot and label. The transmitters are shown using the red dots, annotated with the respective transmission frequency.

334

#### 4.2 Accounting for D-Region Non-Stationarity

335

336

337

338

339

340

341

342

343

344

345

346

347

348

349

350

351

352

In order to discern variations and trends in the measured D-region roughness metrics, the time series of all the data collected must be subsampled into smaller windows to increase the number of available observations. The optimal window size is one that has the smallest possible size, while maintaining stable stochastic properties. The first check is to test the stationarity of the process being detected. Stationarity is often an underlying assumption in time series analysis and enables the use of many simplifications. The two most common types of stationarity are: 1) *Strict-Sense Stationary* (SSS) and 2) *Wide-Sense Stationary* (WSS), see (Durgin, 2002). Unfortunately, it was found that the data collected from the data campaigns is not WSS, and thus not SSS, which aligns with literature since it is well known that the nighttime D-region is highly erratic, e.g. (Thomson et al., 2007). However, a meaningful method is needed to determine an (approximately) optimal window size to use to segment the data collected from the field campaigns. The work by (Arikan & Erol, 1998) discusses methods for determining a proper window size for sliding window statistics where the process will be “locally stationary”, specifically in the context of ionospheric remote sensing. An empirical method described in this work is to inspect the data around the calculated sliding window mean,  $\mu$ , for different window sizes and select the longest window for which most of the data lies within a standard deviation,  $\sigma$ , of the mean.

353

354

355

356

357

358

359

360

361

Analogous to above, increasing the window size used for a cross-correlation, the metric of interest, would increase its fidelity, but decrease its sensitivity to temporal variations. Thus, a proper window size would be as long as possible, while maintaining temporal sensitivity. This can be empirically found as the shortest window size that just stabilizes the variation in the correlation length scale. Figure 6 shows the change in correlation length scale as a function of time and window size. The top panel shows the major axis correlation length, where each line represents a different window size as noted in the legend. The red dashed line is the correlation length for the entire time series. Each point in each line corresponds to the start time of the window used. The bottom panel

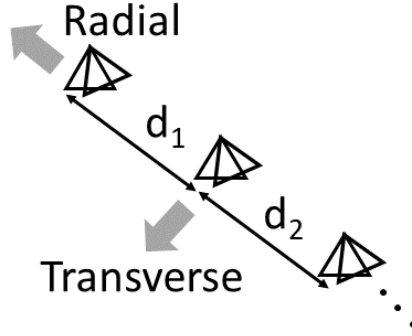


**Figure 5.** Orientation reference for the spaced receivers where the arrow indicates the direction towards the transmitter being detected.

362 shows the minor axis correlation length. It is evident from the figure that the correla-  
 363 tion length scales in both the major and minor axis begin to converge around 25 min-  
 364 utes. Window overlapping can also be used in order to maximize the length of each win-  
 365 dow and the number of windows. Ultimately, a window size of 20 minutes with a 2.5-  
 366 minute overlap (on each end) is used.

### 367 4.3 Roughness Metrics

368 Using a window and overlap size of  $20 \pm 2.5$  minutes, as determined in the pre-  
 369 vious section, all the collected field campaign data can be segmented and analyzed. This  
 370 section will focus on the “horizontal roughness”, namely the correlation length scale. Fig-  
 371 ure 7 summarizes all the collected field campaign data. The data is segmented by ma-  
 372 jor and minor axis and by the orientation of the antenna array in regard to the trans-  
 373 mitter being detected. Recall that “radial” refers to the array being parallel to the path  
 374 of propagation and “transverse” refers to the array being perpendicular to the path of  
 375 propagation. In each of the four panels a histogram of the correlation length scale, nor-  
 376 malized by the wavenumber according to Equation 15, is shown with the y-axis indicat-  
 377 ing the probability density function, or PDF. The geometric mean and standard devi-  
 378 ation are shown in the top right corner of each panel. The black line over each histogram  
 379 is a best fit Rician distribution meant to capture the shape and trend of the distribu-  
 380 tion of each data set. The most pronounced trend in the figure is the difference between  
 381 the major and minor axis correlation lengths in terms of the shapes, i.e. mean and stan-  
 382 dard deviation, of the distributions. The differences between the radial and transverse  
 383 distributions, for both the major and minor axis, are a lot more subtle. This may sug-  
 384 gest that the major axis, or  $H_\phi$ , is sensitive to a different scattering mechanism than the  
 385 minor axis, or  $H_\theta$ .

$$kL = \frac{2\pi}{\lambda} L \quad (15)$$

386 Another way of interpreting the data in Figure 7 is in reference to the estimated  
 387 Fresnel zone size for the respective dimension. Figure 8 shows the same data as in Fig-  
 388 ure 7, but normalized by the Fresnel zone. Due to the long propagation paths used, the  
 389 radial dimension of the Fresnel zone is much larger than the transverse dimension, with  
 390 the latter remaining consistent. This property can be observed in the two left panels of  
 391 the figure, the radial orientations, which have different shapes than those in Figure 7,  
 392 but the right panels, the transverse orientation, remained fairly consistent. In literature,

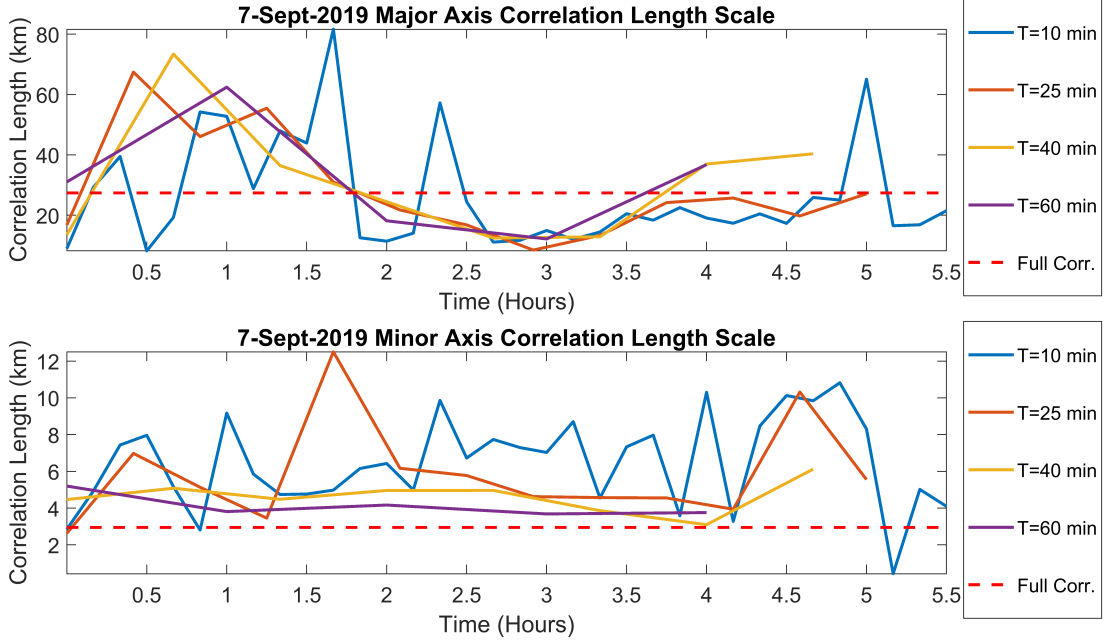


**Figure 6.** Superposition of the correlation length scale, as a function of time, calculated for varying window sizes. The top panel shows the major axis correlation length and the bottom panel shows the minor axis correlation length.

393 the ratio of the correlation length and the Fresnel zone is used to determine what, if any,  
 394 approximations can be made to model scattering. The work done by (Spetzler & Snieder,  
 395 2001b), (Spetzler & Snieder, 2001a), and (Spetzler et al., 2002) investigated when it was  
 396 appropriate to use ray theory versus scattering theory based on this ratio, which can be  
 397 used to provide a sense of scale of roughness. The correlation length scale can be thought  
 398 of as a proxy for the scale of the perturbation, (Bowles et al., 1963), or rather the re-  
 399 sulting angular spreading of the signal, (Bramley, 1951) and (Lindner, 1975a). If the pri-  
 400 mary scattering mechanism is attributed to some number of small irregularities, then the  
 401 correlation length scale is expected to be smaller than the Fresnel zone, (R. J. Doviak  
 402 & Zrnica, 1983). If the correlation length scale is larger than the Fresnel zone, then it is  
 403 suggested that a larger-scale structure is causing the scattering. The radial major axis,  
 404 top left panel, and minor axis values, two bottom panels, both fall in the regime of “scat-  
 405 tering theory”, i.e.  $\frac{L}{L_F} < 1$ , while the top right panel, the case of the transverse ma-  
 406 jor axis, falls partly in the regime of “ray theory”, i.e.  $\frac{L}{L_F} \gg 1$ .

407 Once more using the window size and overlap of  $20 \pm 2.5$  minutes, the data is seg-  
 408 mented and analyzed to investigate the vertical roughness. Figure 9 summarizes all the  
 409 collected field campaign data. The data is segmented by the orientation of the antenna  
 410 array in regard to the transmitter being detected – radial and transverse. In each panel  
 411 a histogram of the RMS height variation, normalized by the wavenumber according to  
 412 Equation 16, is shown with the y-axis indicating the probability density function, or PDF.  
 413 The geometric mean and standard deviation are shown in the top right corner of each  
 414 panel. The black line over each histogram is a best fit Rician distribution meant to cap-  
 415 ture the shape and trend of the distribution of each data set. Unlike the correlation length  
 416 scale data, the variation in the RMS height appears to be a lot lower. In addition, the  
 417 RMS height appears to be consistent across field campaigns, however, as in the case of

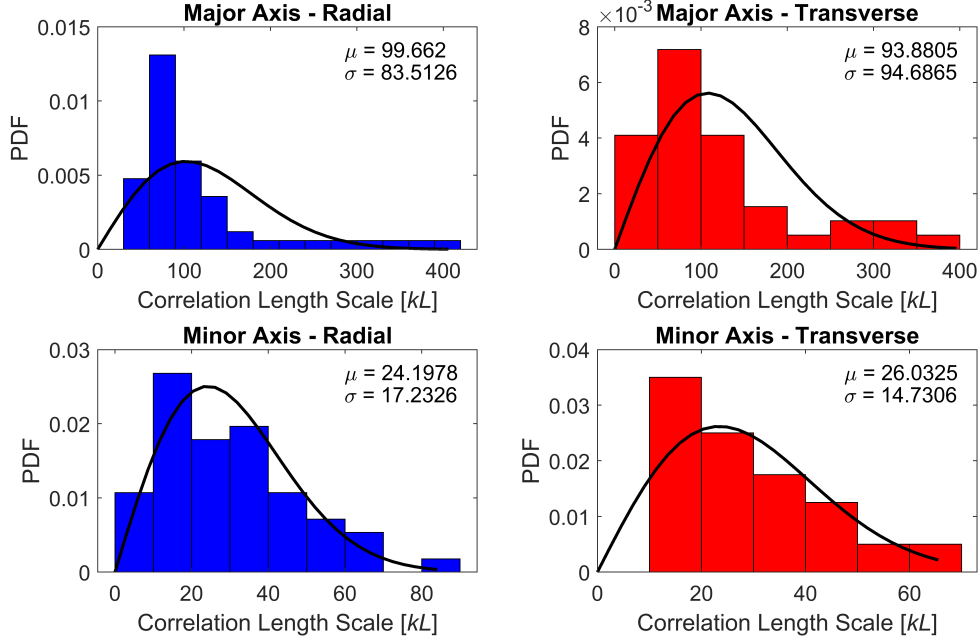


**Figure 7.** Summary of the measured correlation length scale values for all field campaigns. Top left panel: Major axis correlation length scale for the radial direction. Top right panel: Major axis correlation length scale for the transverse direction. Bottom left panel: Minor axis correlation length scale for the radial direction. Bottom right panel: Minor axis correlation length scale for the transverse direction.

418 the correlation length scale, more data must be collected in order to determine any sea-  
 419 sonal trends.

$$k\sigma = \frac{2\pi}{\lambda}\sigma \quad (16)$$

#### 420 4.4 Comparison to VLF Transmitters

421 Using a Very Low Frequency (VLF) transmitter on a similar path to a LF/MF NDGPS  
 422 transmitter, the above roughness metrics can be studied as a function of frequency. This  
 423 comparison can be done using the data collected on the 7-September-2019 field campaign  
 424 in Baxley, Georgia, for the VLF transmitter in North Dakota, call sign “NML”, and the  
 425 NDGPS transmitter in Detroit, Michigan. Figure 10 shows the transmitter-receiver ge-  
 426 ometry (red lines) between Baxley, Georgia, (blue dot) and the two transmitters (red dots).  
 427 The Detroit NDGPS transmitter is located approximately 1151.7 km from Baxley (GA)  
 428 in a North-South path and transmits at 319 kHz. The NML transmitter is located ap-  
 429 proximately 2104.7 km from Baxley (GA) in a more Northwest-Southeast path and trans-  
 430 mits at 25.2 kHz. Although the NML-to-Baxley path is not an ideal comparison to the  
 431 Detroit-to-Baxley path, it can serve as a useful proxy for investigating how the rough-  
 432 ness metrics vary with frequency.

433 First, using the same window and overlap size of  $20 \pm 2.5$  minutes, the horizon-  
 434 tal roughness, or correlation length scale, is investigated. Figure 11 summarizes the cor-  
 435 relation length scale data for both transmitters. The two left panels show the data for  
 436 the NDGPS transmitter. The top panel shows the major axis correlation length scale

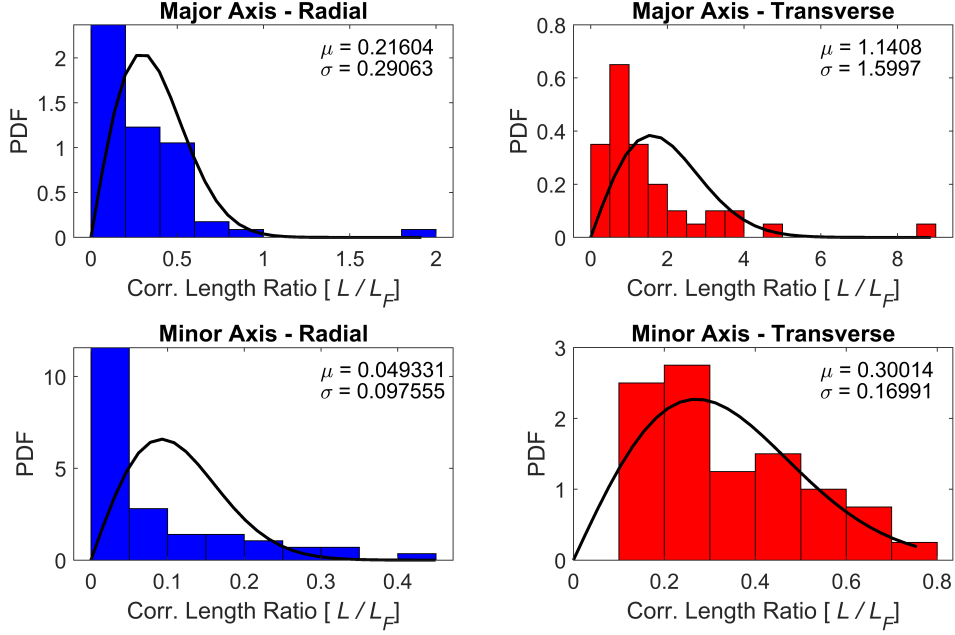


**Figure 8.** Summary of the measured correlation length scale values for all field campaigns normalized by their approximate Fresnel zone dimensions. Top left panel: Major axis correlation length scale for the radial direction. Top right panel: Major axis correlation length scale for the transverse direction. Bottom left panel: Minor axis correlation length scale for the radial direction. Bottom right panel: Minor axis correlation length scale for the transverse direction.

437 data and the bottom panel shows the minor axis correlation length scale data. The right  
 438 panels show the data for the VLF transmitter. The top panel shows the major axis cor-  
 439 relation length scale data and the bottom panel shows the minor axis correlation length  
 440 scale data. Once more, in each panel, the mean,  $\mu$ , and standard deviation,  $\sigma$ , are show  
 441 in the top right corner and the black line shows the best fit Rician to give a sense of the  
 442 shape of the distribution. All values are normalized by the *wavenumber* of the respec-  
 443 tive transmitter. Between both frequencies, the major and minor axis correlation lengths  
 444 have similar shapes, but there is a significant difference in the magnitudes of the cor-  
 445 relation length values. The NDGPS transmitter values tend to be much higher than the  
 446 VLF values, primarily due to the correlation length scales being normalized by the wavenum-  
 447 ber (i.e.  $\propto \frac{1}{\lambda}$ ) of the transmitters, where VLF wavelengths are about  $10\times$  larger than  
 448 LF/MF wavelengths. The normalization gives a reference for how rough the D-region  
 449 is given the wavelength and, in general, the correlation length scale can serve as a proxy  
 450 for the scale of the perturbation, e.g. (Bowles et al., 1963), (Bramley, 1951), and (Lindner,  
 451 1975a). In the case of Figure 11, the major axis correlation length scale measured us-  
 452 ing the NDGPS transmitter is about  $8\times$  larger than that measured by the VLF trans-  
 453 mitter when normalized by the wavenumber,  $3.8\times$  for the minor axis. This suggests that  
 454 the roughness, or perturbations, measured by the NDGPS transmitters were larger, or  
 455 caused more angular spreading, relative to the frequency compared to the VLF trans-  
 456 mitters. This roughly translates to the D-region electron density being measured as “smoother”  
 457 when using VLF. Early work using the partial reflection technique, (Lindner, 1975b), found  
 458 that the angular spreading tended to increase with height. This would be consistent with  
 459 the trend here if it is assumed that the absolute reflection height of the VLF wave is lower  
 460 than the LF/MF wave.

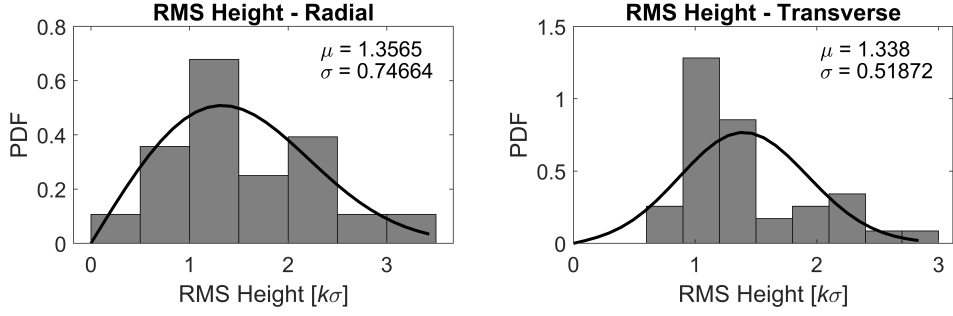


**Figure 9.** Summary of the RMS height variation values for all field campaigns calculated using the differential phase height method. Left panel: RMS height values calculated for the radial orientation. Right panel: RMS height values calculated for the transverse orientation.

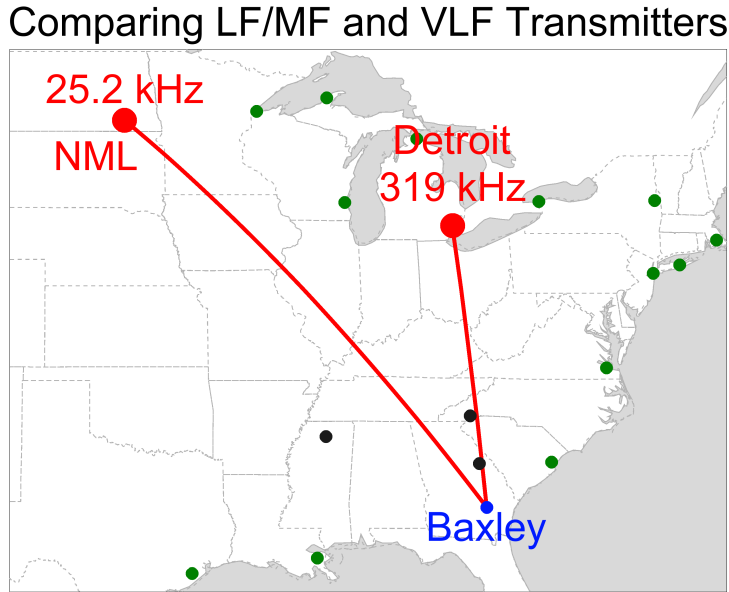


**Figure 10.** Map of the two transmitter-receiver great circle paths (red lines) used to compare the roughness metrics from a VLF transmitter (NML, 25.2 kHz) and an NDGPS transmitter (Detroit (MI), 319 kHz). Data was collected during the 7-September-2019 field campaign in Baxley, Georgia (blue dot).

461 Next, using the same window configuration, the vertical roughness, or RMS height  
 462 variation, is investigated. Figure 12 summarizes the RMS height variation data for both  
 463 transmitters. The left panel shows the data for the NDGPS transmitter. The right panel  
 464 shows the data for the VLF transmitter. In each panel, the mean,  $\mu$ , and standard deviation,  
 465  $\sigma$ , are show in the top right corner and the black line shows the best fit Rician  
 466 to give a sense of the shape of the distribution. All values are normalized by the *wavenum-*  
 467 *ber* of the respective transmitter. Recall that the RMS height variation measured is calculated  
 468 using the *differential phase height* method described in the previous chapter. Thus,  
 469 this is a relative measure between two points in the D-region. Both panels have similar  
 470 shapes, however the left panel mean value, showing the NDGPS transmitter, is about  
 471  $36\times$  larger than the right right panel, VLF transmitter, mean. This suggests that the  
 472 variation in phase height between two points is much higher, relatively to a wavelength,

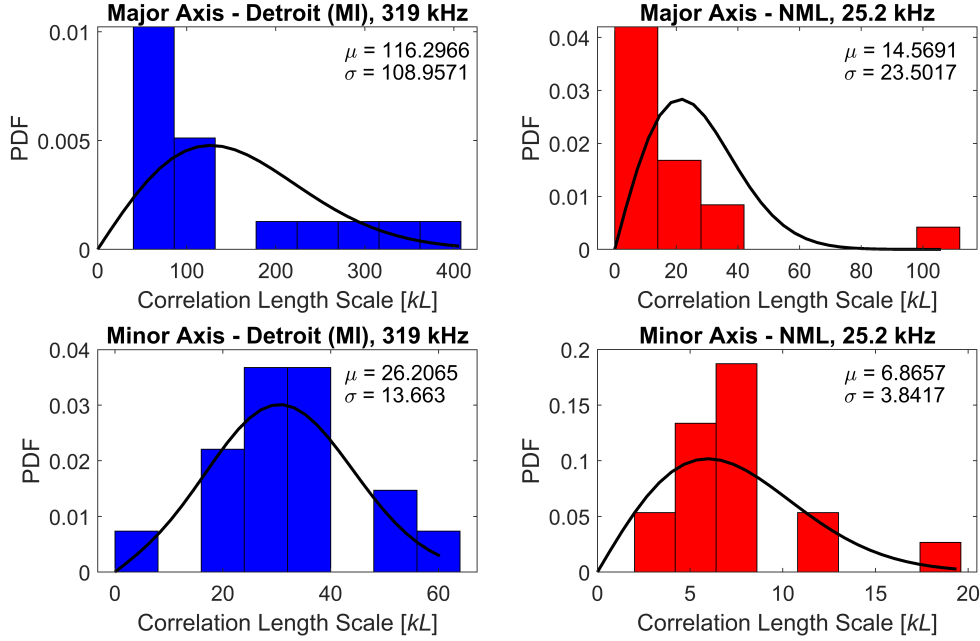


**Figure 11.** Summary of the correlation length scale values from the 7-September-2019 field campaign calculated in the radial direction. Left panels: Major axis (top) and minor axis (bottom) correlation length scales calculated for the NDGPS transmitter in Detroit (MI) transmitting at 319 kHz at a distance of 1151.7 km. Right panel: Major axis (top) and minor axis (bottom) correlation length scales calculated for the VLF transmitter “NML” transmitting at 25.2 kHz at a distance of 2104.7 km.

473 for an LF/MF wave than for a VLF wave. This is consistent with the correlation length  
 474 scale measurement in suggesting that the D-region appears “smoother” for the VLF trans-  
 475 mitter.

## 476 5 Conclusion

477 In this paper we present a method of characterizing the horizontal and vertical elec-  
 478 tron density roughness of the D-region ionosphere using Nationwide Differential GPS (NDGPS)  
 479 transmitters as Low Frequency (LF; 30–300 kHz) and Medium Frequency (MF; 300–3000  
 480 kHz) signals of opportunity. The horizontal roughness is characterized using an ampli-  
 481 tude cross-correlation method, which yields the correlation length scale metric. The ver-  
 482 tical roughness is characterized using a differential phase height, which is needed to mit-  
 483 igate the effects of transmitter phase instability. The ranges and typical values of rough-  
 484 ness metrics are investigated using data from several field campaign measurements. Fi-  
 485 nally, the roughness metrics for an NDGPS transmitter and VLF transmitter are com-  
 486 pared. It is found that the roughness detected by the VLF transmitter is significantly  
 487 smoother and demonstrates the utility of this method to complement traditional VLF  
 488 measurements.

## 489 Acknowledgments

490 This work was supported by the National Science Foundation under grant AGS 1451142  
 491 and AGS 1653114 (CAREER) to the Georgia Institute of Technology. The first author’s

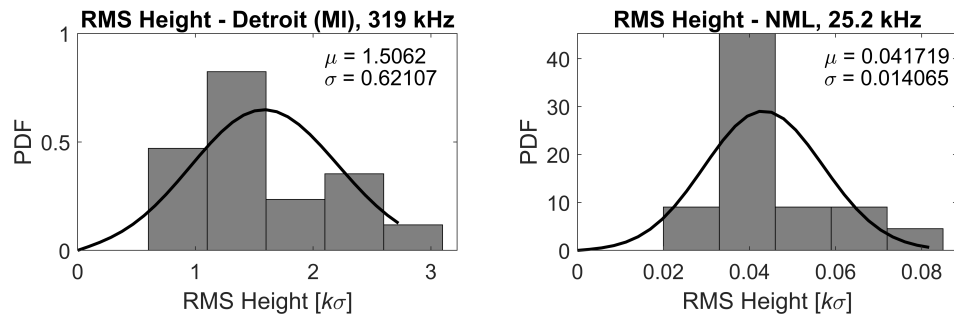


**Figure 12.** Summary of the RMS height variation values from the 7-September-2019 field campaign calculated using the differential phase height method in the radial direction. Left panel: RMS height values calculated for the NDGPS transmitter in Detroit (MI) transmitting at 319 kHz at a distance of 1151.7 km. Right panel: RMS height values calculated for the VLF transmitter “NML” transmitting at 25.2 kHz at a distance of 2104.7 km.

492 work was also supported by the NSF Graduate Research Fellowship, DGE 1650044. Data  
493 will be made available through the WALDO repository (<http://waldo.world/>).

## 494 References

- 495 Arikian, F., & Erol, C. B. (1998). Statistical characterization of time variability in  
496 midlatitude single-tone HF channel response. *Radio Science*, *33*(5), 1429–1443.  
497 doi: 10.1029/98RS01889
- 498 Belrose, J., Hatton, W., McKerrow, C., & Thain, R. (1959, may). The Engineer-  
499 ing of Communication Systems for Low Radio Frequencies. *Proceedings of*  
500 *the IRE*, *47*(5), 661–680. Retrieved from [http://ieeexplore.ieee.org/](http://ieeexplore.ieee.org/document/4065729/)  
501 [document/4065729/](http://ieeexplore.ieee.org/document/4065729/) doi: 10.1109/JRPROC.1959.287236
- 502 Belrose, J., & Thomas, L. (1968, jan). Ionization changes in the middle lat-  
503 titude D-region associated with geomagnetic storms. *Journal of Atmo-*  
504 *spheric and Terrestrial Physics*, *30*(7), 1397–1413. Retrieved from [https://](https://www.sciencedirect.com/science/article/pii/S0021916968912609)  
505 [www.sciencedirect.com/science/article/pii/S0021916968912609](https://www.sciencedirect.com/science/article/pii/S0021916968912609) doi:  
506 10.1016/S0021-9169(68)91260-9
- 507 Bickel, J. E. (1957, sep). A method for obtaining LF oblique-incidence reflection  
508 coefficients and its application to 135.6-kc/s data in the Alaskan area. *Journal*  
509 *of Geophysical Research*, *62*(3), 373–381. Retrieved from [http://doi.wiley](http://doi.wiley.com/10.1029/JZ062i003p00373)  
510 [.com/10.1029/JZ062i003p00373](http://doi.wiley.com/10.1029/JZ062i003p00373) doi: 10.1029/JZ062i003p00373
- 511 Bowles, K. L., Balsley, B. B., & Cohen, R. (1963, may). Field-aligned E -region ir-  
512 regularities identified with acoustic plasma waves. *Journal of Geophysical Re-*  
513 *search*, *68*(9), 2485–2501. doi: 10.1029/jz068i009p02485
- 514 Bramley, E. (1951, jan). Diversity effects in spaced-aerial reception of ionospheric  
515 waves. *Proceedings of the IEE - Part III: Radio and Communication Engineer-*  
516 *ing*, *98*(51), 19–25. Retrieved from [https://digital-library.theiet.org/](https://digital-library.theiet.org/content/journals/10.1049/pi-3.1951.0004)  
517 [content/journals/10.1049/pi-3.1951.0004](https://digital-library.theiet.org/content/journals/10.1049/pi-3.1951.0004) doi: 10.1049/pi-3.1951.0004
- 518 Briggs, B. H., Phillips, G. J., & Shinn, D. H. (1950). The analysis of observations on  
519 spaced receivers of the fading of radio signals. *Proceedings of the Physical Soci-*  
520 *ety. Section B*, *63*(2), 106–121. doi: 10.1088/0370-1301/63/2/305
- 521 Clarke, C. (1962). Atmospheric radio-noise studies based on amplitude-probability  
522 measurements at Slough, England, during the International Geophys-  
523 ical Year. *Proceedings of the IEE Part B: Electronic and Communication*  
524 *Engineering*, *109*(47), 393. Retrieved from <http://digital-library>

- 525 .theiet.org/content/journals/10.1049/pi-b-2.1962.0224 doi:  
526 10.1049/pi-b-2.1962.0224
- 527 Cohen, M. B., Said, R. K., Paschal, E. W., McCormick, J. C., Gross, N. C., Thomp-  
528 son, L., ... Chang, J. (2018, sep). Broadband longwave radio remote sens-  
529 ing instrumentation. *Review of Scientific Instruments*, 89(9), 094501. Re-  
530 trieved from <http://aip.scitation.org/doi/10.1063/1.5041419> doi:  
531 10.1063/1.5041419
- 532 Doviak, J., Lataitis, J., Holloway, L., & Van Baelen, J. (1994). A Generalized The-  
533 oretical Analysis of Cross-correlation and Cross-spectra for Spaced-antenna  
534 Wind Profilers.  
535 doi: 10.5065/D6N014G4
- 536 Doviak, R. J., & Zrnica, D. S. (1983). Fresnel zone considerations for reflection and  
537 scatter from refractive index irregularities. In *Conference on radar meteorology*  
538 *of the american meteorological society* (pp. 111–117). Retrieved from [https://](https://ntrs.nasa.gov/search.jsp?R=19840019023)  
539 [ntrs.nasa.gov/search.jsp?R=19840019023](https://ntrs.nasa.gov/search.jsp?R=19840019023)
- 540 Durgin, G. (2002). Space-Time Wireless Channels. *Space-Time Wireless*  
541 *Channels*, 1–19. Retrieved from [https://books.google.com/books?hl=](https://books.google.com/books?hl=en&lr=&id=6sK3nYBoUmAC&oi=fnd&pg=PR15&dq=space-time+wireless+channels+durgin&ots=BN6cL53cgX&sig=P{\_}6I2rPJzyIBJcFmraAWHucPcshttp://www.ncbi.nlm.nih.gov/pubmed/23834000)  
542 [en{\&}lr={\&}id=6sK3nYBoUmAC{\&}oi=fnd{\&}pg=PR15{\&}dq=space](https://books.google.com/books?hl=en&lr=&id=6sK3nYBoUmAC&oi=fnd&pg=PR15&dq=space-time+wireless+channels+durgin&ots=BN6cL53cgX&sig=P{\_}6I2rPJzyIBJcFmraAWHucPcshttp://www.ncbi.nlm.nih.gov/pubmed/23834000)  
543 [-time+wireless+channels+durgin{\&}ots=BN6cL53cgX{\&}sig=P{\](https://books.google.com/books?hl=en&lr=&id=6sK3nYBoUmAC&oi=fnd&pg=PR15&dq=space-time+wireless+channels+durgin&ots=BN6cL53cgX&sig=P{\_}6I2rPJzyIBJcFmraAWHucPcshttp://www.ncbi.nlm.nih.gov/pubmed/23834000)  
544 [\\_}6I2rPJzyIBJcFmraAWHucPcshttp://www.ncbi.nlm.nih.gov/pubmed/](https://books.google.com/books?hl=en&lr=&id=6sK3nYBoUmAC&oi=fnd&pg=PR15&dq=space-time+wireless+channels+durgin&ots=BN6cL53cgX&sig=P{\_}6I2rPJzyIBJcFmraAWHucPcshttp://www.ncbi.nlm.nih.gov/pubmed/23834000)  
545 [23834000](https://books.google.com/books?hl=en&lr=&id=6sK3nYBoUmAC&oi=fnd&pg=PR15&dq=space-time+wireless+channels+durgin&ots=BN6cL53cgX&sig=P{\_}6I2rPJzyIBJcFmraAWHucPcshttp://www.ncbi.nlm.nih.gov/pubmed/23834000) doi: 10.1300/J155v04n04\_01
- 546 Füllekrug, M., Koh, K., Liu, Z., & Mezentsev, A. (2019, jan). First Map of Co-  
547 herent Low-Frequency Continuum Radiation in the Sky. *Radio Science*, 54(1),  
548 44–59. Retrieved from <http://doi.wiley.com/10.1029/2018RS006705> doi:  
549 10.1029/2018RS006705
- 550 Füllekrug, M., Smith, N., Mezentsev, A., Watson, R., Astin, I., Gaffet, S., ...  
551 Rycroft, M. (2015, nov). Multipath propagation of low-frequency radio  
552 waves inferred from high-resolution array analysis. *Radio Science*, 50(11),  
553 1141–1149. Retrieved from <http://doi.wiley.com/10.1002/2015RS005781>  
554 doi: 10.1002/2015RS005781
- 555 Gross, N. C., Cohen, M. B., Said, R. K., & Gołkowski, M. (2018, jan). Polar-  
556 ization of Narrowband VLF Transmitter Signals as an Ionospheric Diag-  
557 nostic. *Journal of Geophysical Research: Space Physics*, 123(1), 901–917.  
558 Retrieved from <http://doi.wiley.com/10.1002/2017JA024907> doi:  
559 10.1002/2017JA024907
- 560 Higginson-Rollins, M. A., & Cohen, M. B. (2017, aug). Exploiting LF/MF sig-  
561 nals of opportunity for lower ionospheric remote sensing. *Geophysical Research*  
562 *Letters*, 44(16), 8665–8671. Retrieved from [http://doi.wiley.com/10.1002/](http://doi.wiley.com/10.1002/2017GL074236)  
563 [2017GL074236](http://doi.wiley.com/10.1002/2017GL074236) doi: 10.1002/2017GL074236
- 564 Higginson-Rollins, M. A., & Cohen, M. B. (2020). Studying the Effects of the Au-  
565 gust 2017 Solar Eclipse using LF/MF Signals of Opportunity.  
566 doi: 10.1002/ESSOAR.10502560.1
- 567 Hocking, W. (1987, nov). Reduction of the effects of non-stationarity in stud-  
568 ies of amplitude statistics of radio wave backscatter. *Journal of Atmo-*  
569 *spheric and Terrestrial Physics*, 49(11-12), 1119–1131. Retrieved from  
570 <https://www.sciencedirect.com/science/article/pii/0021916987900948>  
571 doi: 10.1016/0021-9169(87)90094-8
- 572 Hocking, W. K. (1979). Angular and temporal characteristics of partial reflections  
573 from the D-region of the ionosphere. *Journal of Geophysical Research*, 84(A3),  
574 845. doi: 10.1029/ja084ia03p00845
- 575 Kotovsky, D. A., & Moore, R. C. (2016, may). Photochemical response of the  
576 nighttime mesosphere to electric field heating-Onset of electron density en-  
577 hancements. *Journal of Geophysical Research: Space Physics*, 121(5), 4782–  
578 4799. Retrieved from <http://doi.wiley.com/10.1002/2015JA022054> doi:  
579 10.1002/2015JA022054

- 580 Last, D., & Poppe, D. (1996, dec). A Coverage Prediction Model for Radio Beacon  
581 Differential Satellite Navigation Systems. *Navigation*, 43(4), 451–469. Re-  
582 trieved from <http://doi.wiley.com/10.1002/j.2161-4296.1996.tb01932.x>  
583 doi: 10.1002/j.2161-4296.1996.tb01932.x
- 584 Last, J., & Poppe, D. (1997). Effect of skywave interference on coverage of ra-  
585 diobeacon DGPS stations. *IEEE Proceedings - Radar, Sonar and Navigation*,  
586 144(3), 163. Retrieved from [http://digital-library.theiet.org/content/  
587 journals/10.1049/ip-rsn{\\\_}19971177](http://digital-library.theiet.org/content/journals/10.1049/ip-rsn{\_}19971177) doi: 10.1049/ip-rsn:19971177
- 588 Lay, E. H., & Shao, X. M. (2011a, jan). High temporal and spatial - resolution  
589 detection of D - layer fluctuations by using time - domain lightning wave-  
590 forms. *Journal of Geophysical Research: Space Physics*, 116(January), 1–  
591 8. Retrieved from <http://doi.wiley.com/10.1029/2010JA016018> doi:  
592 10.1029/2010JA016018
- 593 Lay, E. H., & Shao, X. M. (2011b, dec). Multi-station probing of thunderstorm-  
594 generated D-layer fluctuations by using time-domain lightning waveforms. *Geo-  
595 physical Research Letters*, 38(23), n/a–n/a. Retrieved from [http://doi.wiley  
596 .com/10.1029/2011GL049790](http://doi.wiley.com/10.1029/2011GL049790) doi: 10.1029/2011GL049790
- 597 Lindner, B. (1975a). The Nature of D-region Scattering of Vertical Incidence Radio  
598 Waves. I. Generalized Statistical Theory of Diversity Effects Between Spaced  
599 Receiving Antennas. *Australian Journal of Physics*, 28(2), 163. Retrieved from  
600 <http://www.publish.csiro.au/?paper=PH750163> doi: 10.1071/PH750163
- 601 Lindner, B. (1975b). The Nature of D-region Scattering of Vertical Incidence Radio  
602 Waves. II. Experimental Observations Using Spaced Antenna Reception. *Aus-  
603 tralian Journal of Physics*, 28(2), 171. Retrieved from [http://www.publish  
604 .csiro.au/?paper=PH750171](http://www.publish.csiro.au/?paper=PH750171) doi: 10.1071/PH750171
- 605 Mathews, J. D., Shapiro, J. H., & Tanenbaum, B. S. (1973, dec). Evidence for dis-  
606 tributed scattering in D region partial-reflection processes. *Journal of Geophys-  
607 ical Research*, 78(34), 8266–8275. Retrieved from [http://doi.wiley.com/10  
608 .1029/JA078i034p08266](http://doi.wiley.com/10.1029/JA078i034p08266) doi: 10.1029/JA078i034p08266
- 609 McCormick, J. C., Cohen, M. B., Gross, N. C., & Said, R. K. (2018, apr). Spa-  
610 tial and Temporal Ionospheric Monitoring Using Broadband Sferic Mea-  
611 surements. *Journal of Geophysical Research: Space Physics*, 123(4), 3111–  
612 3130. Retrieved from <http://doi.wiley.com/10.1002/2017JA024291> doi:  
613 10.1002/2017JA024291
- 614 McKerrow, C. (1957). Some Recent Measurements of Atmospheric Noise in Canada.  
615 *Proceedings of the IRE*, 45(6), 782–786. Retrieved from [http://ieeexplore  
616 .ieee.org/document/4056602/](http://ieeexplore.ieee.org/document/4056602/) doi: 10.1109/JRPROC.1957.278475
- 617 McKerrow, C. A. (1960, jul). Some measurements of atmospheric noise levels  
618 at low and very low frequencies in Canada. *Journal of Geophysical Re-  
619 search*, 65(7), 1911–1926. Retrieved from [http://doi.wiley.com/10.1029/  
620 JZ065i007p01911](http://doi.wiley.com/10.1029/JZ065i007p01911) doi: 10.1029/JZ065i007p01911
- 621 Nicolet, M., & Aikin, A. C. (1960, may). The formation of the D region of  
622 the ionosphere. *Journal of Geophysical Research*, 65(5), 1469–1483. Re-  
623 trieved from <http://doi.wiley.com/10.1029/JZ065i005p01469> doi:  
624 10.1029/JZ065i005p01469
- 625 P. Beckmann, & A. Spizzichino. (1963). *The Scattering of Electromagnetic Waves  
626 from Rough Surfaces*. New York: Pergamon Press.
- 627 Piggott, W. R., Pitteway, M. L. V., & Thrane, E. V. (1965, mar). The Numerical  
628 Calculation of Wave-Fields, Reflexion Coefficients and Polarizations for Long  
629 Radio Waves in the Lower Ionosphere. II. *Philosophical Transactions of the  
630 Royal Society A: Mathematical, Physical and Engineering Sciences*, 257(1079),  
631 243–271. doi: 10.1098/rsta.1965.0005
- 632 Ratcliffe, J. A. (1956). Some aspects of diffraction theory and their application to  
633 the ionosphere. *Reports on Progress in Physics*, 19(1), 188–267. doi: 10.1088/  
634 0034-4885/19/1/306

- 635 Shapiro, J. H. (1973, may). Statistical models for D-region partial-reflection experi-  
636 ments. *Radio Science*, 8(5), 431–435. Retrieved from [http://doi.wiley.com/](http://doi.wiley.com/10.1029/RS008i005p00431)  
637 [10.1029/RS008i005p00431](http://doi.wiley.com/10.1029/RS008i005p00431) doi: 10.1029/RS008i005p00431
- 638 Spetzler, J., Sivaji, C., Nishizawa, O., & Fukushima, Y. (2002). A test of  
639 ray theory and scattering theory based on a laboratory experiment us-  
640 ing ultrasonic waves and numerical simulation by finite-difference method.  
641 *Geophysical Journal International*, 148(2), 165–178. Retrieved from  
642 <https://academic.oup.com/gji/article-abstract/148/2/165/596588>  
643 doi: 10.1046/j.1365-246X.2002.01552.x
- 644 Spetzler, J., & Snieder, R. (2001a). The effect of small-scale heterogeneity on the  
645 arrival time of waves. *Geophysical Journal International*, 145(3), 786–796.  
646 Retrieved from [https://academic.oup.com/gji/article-abstract/145/3/](https://academic.oup.com/gji/article-abstract/145/3/786/648126)  
647 [786/648126](https://academic.oup.com/gji/article-abstract/145/3/786/648126) doi: 10.1046/j.1365-246X.2001.01438.x
- 648 Spetzler, J., & Snieder, R. (2001b). The formation of caustics in two-and three-  
649 dimensional media. *Geophysical Journal International*, 144(1), 175–182.  
650 Retrieved from [https://academic.oup.com/gji/article-abstract/144/1/](https://academic.oup.com/gji/article-abstract/144/1/175/764650)  
651 [175/764650](https://academic.oup.com/gji/article-abstract/144/1/175/764650) doi: 10.1046/j.1365-246X.2001.00308.x
- 652 Thomson, N. R., Clilverd, M. A., & McRae, W. M. (2007, jul). Nighttime iono-  
653 spheric D region parameters from VLF phase and amplitude. *Journal of Geo-*  
654 *physical Research: Space Physics*, 112(7), n/a–n/a. Retrieved from [http://](http://doi.wiley.com/10.1029/2007JA012271)  
655 [doi.wiley.com/10.1029/2007JA012271](http://doi.wiley.com/10.1029/2007JA012271) doi: 10.1029/2007JA012271
- 656 Wernik, A. W., Liu, C. H., & Yeh, K. C. (1983). Modeling of spaced-receiver  
657 scintillation measurements. *Radio Science*, 18(5), 743–764. doi: 10.1029/  
658 [RS018i005p00743](http://doi.wiley.com/10.1029/RS018i005p00743)
- 659 Wolfe, D. B., Judy, C. L., Haukkala, E. J., & Godfrey, D. J. (2000). Engineering  
660 The World’s Largest DGPS Network. *Control Engineering*, 1(June), 26–28.  
661 Retrieved from <http://ieeexplore.ieee.org/document/881237/> doi:  
662 [10.1109/OCEANS.2000.881237](http://ieeexplore.ieee.org/document/881237/)